Inorganic Chemistry
Cite This: Inorg. Chem. 2019, 58, 637−647
Article
pubs.acs.org/IC

Electronic, Magnetic, and Theoretical Characterization of $(NH_4)_4UF_8$, a Simple Molecular Uranium(IV) Fluoride

Alexander T. Chemey,[†] Cristian Celis-Barros,[†] Kevin Huang,[‡] Joseph M. Sperling,[†] Cory J. Windorff,[†] Ryan E. Baumbach,[‡,§] David E. Graf,*[,‡] Dayán Páez-Hernández,[∥] Michael Ruf,[⊥] David E. Hobart,[†] and Thomas E. Albrecht-Schmitt*[,†]

[†]Department of Chemistry and Biochemistry, Florida State University, Tallahassee, Florida 32306, United States
[‡]National High Magnetic Field Laboratory, Florida State University, Tallahassee, Florida 32306, United States
[§]Department of Physics, Florida State University, Tallahassee, Florida 32306, United States
[∥]Centro de Nanociencias Aplicadas, Facultad de Ciencias Exactas, Universidad Andrés Bello, Republica 275, Santiago, Chile
[⊥]Bruker AXS, 5465 East Cheryl Parkway, Madison, Wisconsin 53711, United States

Supporting Information

ABSTRACT: The simple system of tetraammonium octafluorouranate is employed to derive a fundamental understanding of the uranium−fluorine interaction. The structure is composed of isolated molecules, enabling a detailed examination of the U^{4+} (f^2) ion. Characterization of single-crystals by X-ray diffraction, absorption spectroscopy, and magnetic analysis up to 45 T is combined with extensive theoretical treatment by CASSCF. The influence of different active spaces and representations of the structure is examined in the context of the experimental evidence. The Interacting Quantum Atoms method (IQA) is used to examine the nature of the U−F bond, concluding that there is a non-negligible degree of covalent character (9% of the total bond energy) in $[UF_8]^{4-}$. For the structural and theoretical reasons discussed herein, it is proposed that the structure of $(NH_4)_4UF_8$ may be appropriately employed as a benchmark compound for future theoretical characterization of U(IV).

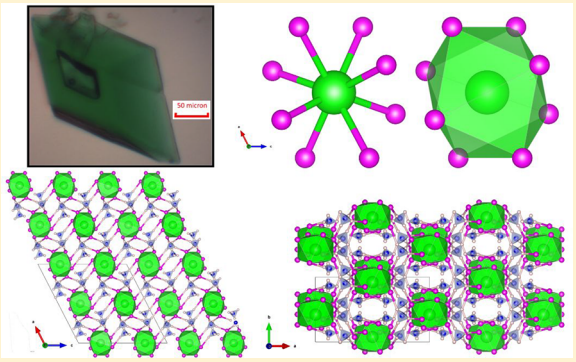

INTRODUCTION

Understanding the interactions between the actinide elements and fluorine has historically been, and remains, vitally important for industrial, scientific, and defense applications of the heaviest elements. The classic chemistry of the actinide series begins with actinide−fluoride interactions, as the lanthanum fluoride method was one of two methods developed by Seaborg and collaborators at the University of Chicago "Met Lab" to separate small amounts of plutonium from fissioned uranium fuel for use in the Manhattan Project.[1] Volatile molecular UF_6 has primarily been used for the enrichment of fissile ^{235}U from natural uranium for use in nuclear fuel.[2−4] Modern interest in molten salt fast reactor designs exploits the relatively low melting points of mixed alkali actinide fluoride salts and beneficial nuclear properties to enable proliferation-resistant nuclear reactors.[5−13] Actinide fluorides are also notably insoluble in even concentrated acids, which has been exploited in recent studies on the convenient isolation of plutonium and curium from complex matrices on a lab scale.[14,15] It is precisely this diverse chemistry that motivates further investigations into the family of actinide fluoride compounds. Moreover, much of the wealth of knowledge of actinide fluoride compounds dates to the Manhattan Project or early Cold War, providing an opportunity to revisit this chemistry with modern instrumentation and theoretical methods.

Compounds of the stoichiometry $(NH_4)_4AnF_8$ (An = Th−Am) were prepared in the 1960s,[16] although the thorium analogue does not share the structure of the later elements.[17,18] Recently, these and similar compounds have been examined for use as precursors to actinide nitrides for nuclear fuel applications.[19−21] Ammonium actinide fluorides have also been used as precursors to pure anhydrous actinide fluorides under both reducing and oxidizing conditions due to the relative volatility of NH_4F from these compounds.[22,23] The plutonium fluoride produced in this manner was historically utilized to produce plutonium metal after reaction with calcium.[22−25] The phase space of ammonium fluoride, uranium tetrafluoride, and water was explored extensively by Penneman and co-workers, who observed at least five stoichiometries and ten phases therein. These studies relied primarily on powder X-ray diffraction methods to identify new phases and thermochemical measurements to assign stoichiometries.

Received: October 1, 2018
Published: December 20, 2018

DOI: 10.1021/acs.inorgchem.8b02800
Inorg. Chem. 2019, 58, 637−647

Table 1. Comparison of Diffraction Data for $(NH_4)_4UF_8$ with the Previously-Reported Structure

	Literature[27]	This Work	
a (Å)	13.126(5)	13.168(2)	13.170(1)
b (Å)	6.692(3)	6.678(1)	6.6487(6)
c (Å)	13.717(5)	13.153(3)	13.093(2)
β (deg)	121.322	117.199(2)	117.238(2)
Volume (Å^3)	1029.29	1028.7(3)	1019.4(2)
Conditions	Room Temperature	230(2) K	150(2) K
U−F distances (Å)	2.25(1)−2.33(1)	2.2611(5)−2.335(5)	2.257(1)−2.335(1)
U−N distances (Å)	4.34(1)−4.60(1)	4.354(5)−4.608(6)	4.344(1)−4.6046(1)
U−U (nearest) (Å)	6.672(2)	6.659(1)	6.6198(6)

This careful work revealed several phases of the form $(NH_4)_x(UF_{4+x})$ ($^1/_3 \leq x \leq 4$).[26] Of the compounds identified, only one, $(NH_4)_4UF_8$ was characterized by single-crystal diffraction,[27] though $(NH_4)_2CeF_6$ was later examined as a surrogate for α-$(NH_4)_2UF_6$.[28]

The structure of $(NH_4)_4UF_8$ was described as isolated UF_8^{4-} antiprisms linked through hydrogen bonds to four ammonium cations.[27] Simple molecular fluorides such as these are uncommon, as only eight of over 50 ternary ($M_xU_yF_z$) and quaternary ($M_wM'_xU_yF_z$) uranium(IV) structures (M, M′ = NH_4^+, group 1−13 metal ions, Ge^{4+}, $Sn^{2+/4+}$, $Pb^{2+/4+}$, $Sb^{3+/5+}$) currently in the Inorganic Crystal Structure Database (ICSD)[29] feature such distinct uranium environments. The remaining structures all feature corner-, edge-, or face-sharing structures and one- to three-dimensional topologies, most of which are held together by μ_2 bridging fluorides.[26,27,30−56] One important exception is UF_6, which sublimes at relatively mild temperature alongside homologue UCl_6, due to weak van der Waals interactions between discrete octahedral molecules.[4,57]

A redetermination of the molecular structure, absorption spectroscopy, high-field magnetic characterization, and theoretical treatment of this convenient model species is presented herein. We also offer a detailed discussion of the electronic structure of this molecule and a discussion of further applicability to the realm of theoretical actinide chemistry.

EXPERIMENTAL SECTION

Synthesis. *Crystallization Strategy 1.* One method described in the literature by Penneman et al.[58] was modified as described below. In a typical reaction, finely powdered turquoise UF_4 (500 mg, 1.59 mmol) (Alfa Inorganics) was placed in a plastic 20 mL vial and dissolved in an aqueous NH_4F solution (20 g, 40% NH_4F w/w) (Sigma-Aldrich, 98%). Immediately a large amount of emerald green $(NH_4)_4UF_8$ precipitated in a powder and formed a solid mass. The supernatant was removed from the precipitate with a plastic pipet and placed into a second vial to precipitate large discrete crystals. Three milliliters of methanol was added to the first vial to remove excess NH_4F from the precipitate and then allowed to dry after removal of the methanol. One milliliter of methanol was also added to the supernatant vial to precipitate single crystals as the vials sat for 2 days undisturbed with their caps off. This method typically yielded many 100 μm-scale green crystals as well as several relatively large (~1 mm × 1 mm × 0.1 mm) dark green parallelepiped crystals. Any remnant supernatant was capped and preserved for liquid-phase absorption spectroscopy.

Crystallization Strategy 2. To produce massive (greater than 1 mg) crystals for magnetic analysis, a vapor diffusion method was employed. The 20 mL plastic vial (approximately 6 cm tall) with dark green supernatant was placed uncapped in a 250 mL polyethylene bottle filled to a depth of less than 3 cm with methanol. The bottle was capped and left undisturbed. After 3−5 days, several single crystals as massive as 11.0 mg were precipitated.

Crystallization Strategy 3. Fluorination of UO_2 by concentrated HF (Sigma-Aldrich, 48 wt %/wt), followed by reaction with NH_4F solution failed to produce crystals. An alternative strategy to produce $(NH_4)_4UF_8$ from UO_2 was found in the literature.[23,24] This reaction of UO_2 (50 mg, 0.16 mmol, Strem) and $NH_4F{\cdot}HF$ (50 mg, 0.88 mmol, Aldrich, 99.999%) was conducted in a High-Density Polyethylene bottle, heated for a week at 100 °C and then cooled to room temperature. Excess ammonium bifluoride was removed by repeatedly rinsing with methanol, followed by evaporation. To produce large single crystals, sufficient 40% weight NH_4F solution was then added to make a concentrated solution of $(NH_4)_4UF_8$ (approximately 0.02 molal).[58] The mixture was allowed to slowly equilibrate at room temperature for at least a week or was shaken on a mechanical shaker plate until a dark green solution formed. The supernatant was removed from any undissolved material and then precipitated with the methanol vapor diffusion method described above.

CAUTION! Although depleted uranium is separated from in-grown daughter products and lower in short-lived ^{235}U ($t_{1/2}$ = 704 million years), ^{238}U ($t_{1/2}$ = 4.468 billion years) remains a radioactive hazard. Fluoride salts such as NH_4F form hydrofluoric acid in contact with water, which is an acute chemical hazard. Reactions were conducted in a fume hood separate from other reactions. Thick HF-safe rubber gloves, a rubber gown, a plastic face shield, and radiation safety equipment were worn, necessitating careful coordination between two experimentalists and extensive practice with analogous reactions.

Single Crystal X-ray Diffraction Studies. Single crystals were isolated from the bulk product and placed under viscous immersion oil. An individual crystal was obtained from under oil with Mitegen tips and then optically aligned on a Bruker D8 Quest X-ray diffractometer using a digital camera. Initial intensity measurements were performed using a IμS X-ray source and a 50 W microfocused sealed tube (Mo Kα, λ = 0.71073 Å) with high-brilliance and high-performance focusing Quazar multilayer optics. Standard APEXIII software was used for determination of the unit cells and data collection control. The intensities of reflections of a hemisphere were collected by a combination of four sets of exposures (frames) at 230 K. Each set had a different φ angle for the crystal, and each exposure covered a range of 0.5 ° in ω. A total of 1464 frames were collected with an exposure time per frame of 30 s at a temperature of 230 K. A total of 2624 frames were collected in a combination of eight sets of exposures (frames) at 150 K. This experiment was optimized for high-redundancy, high-angle data collection up to 0.39 Å resolution with an exposure time of 5 s at a temperature of 150 K. SAINT software was used for data integration including Lorentz and polarization corrections. Semiempirical absorption corrections were applied using the program SCALE (SADABS). The Crystallographic Information Files (CIF) are available from the Cambridge Crystal Structure Database Center with collection numbers 1868290 for 230 K data and 1879530 for 150 K data. A summary of crystallographic results with comparison to the previously reported structure[27] is provided in Table 1. Atomic coordinates and additional structural information for both structures are provided in the Supporting Information, which can be downloaded over the Internet for free at http://pubs.acs.org.

DOI: 10.1021/acs.inorgchem.8b02800
Inorg. Chem. 2019, 58, 637−647

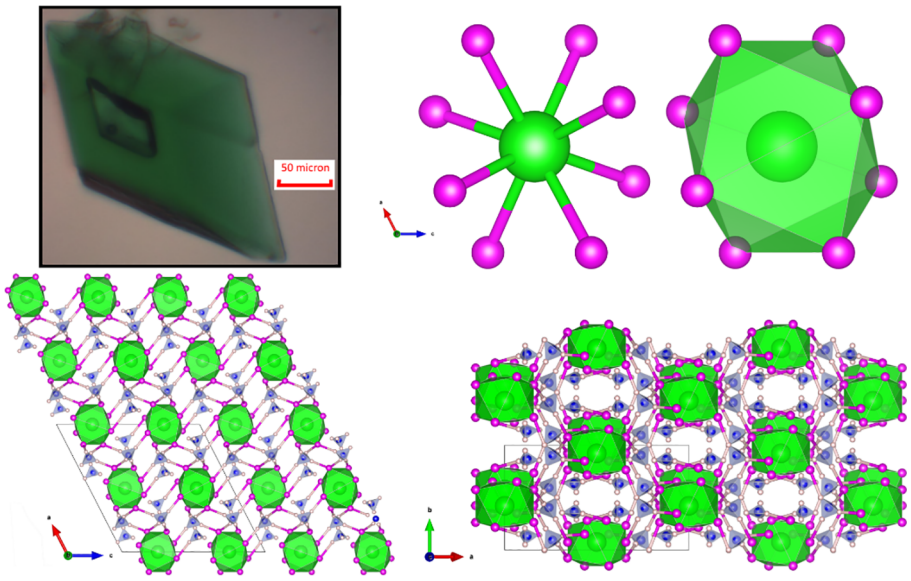

Figure 1. Structure of $(NH_4)_4UF_8$. Clockwise from upper left: A single crystal of $(NH_4)_4UF_8$, the coordination environment of UF_8^{4-}, the view of the packing along the crystallographic *c*-axis, and the distinctive parallelogram packing motif apparent parallel to the crystallographic ac-plane. Color code: green, uranium; pink, fluorine; blue, nitrogen; white, hydrogen.

Absorption Spectra. UV−visible-NIR single-crystal absorption spectra were collected on a glass slide under Krytox oil using a Craic Technologies 20/20 microspectrophotometer. The data were collected with nonpolarized light through the ac-plane from 320 to 1700 nm at room temperature in two collections, from 320 to 1100 nm, and then 1000 to 1700 nm. As the two collections were slightly offset in absorbance, the overlap region was used to adjust the intensity of the near-IR collection to match the UV−visible region. This is critically important due to the strong absorption band centered at 1094.1 nm. The built-in Microsoft Excel Solver Add-in was used to optimize the adjustment with a scale fit of $A = 0.8649A_{NIR} + 0.3136$ and a standard error of the regression of ±0.0010 Abs, where A is the reported relative absorption and A_{NIR} is the near-infrared absorption measurement.[59]

Solution-phase UV−vis-NIR spectra were collected in a 1 cm path length plastic cuvette in aqueous ammonium fluoride solutions on a Cary 6000i spectrometer in the region of 350−1200 nm. Molar absorptivity for the solution spectrum (ε) was determined by a fit line through the background-corrected absorption of six different $(NH_4)_4UF_8$ concentrations in ammonium fluoride solution. Beer's law, $A = \varepsilon bc$, was employed for the five main peaks between 400 and 700 nm.

Magnetic Susceptibility Measurements. Three large dark green crystals (mass = 4.6 mg total) were selected from vapor diffusion crystallizations, quickly dried with methanol, and weighed on filter paper. These crystals were thickly coated in GE Varnish on a diamagnetic quartz half tube, dried in air to harden the varnish, and placed into a diamagnetic plastic tube. A Quantum Design VSM Magnetic Properties Measurement System (MPMS) was used to measure temperature- and field-dependent susceptibility. Temperature-dependent magnetization was observed with both field cooled (0.01 and 1 T) and zero-field cooled experiments from 300 to 2 K, while field-dependent magnetic susceptibility $\chi = M/H$ was examined at 2 K from 0 to 7 T. Further characterization with the 45 T Hybrid Magnet System at the National High Magnetic Field Laboratory was conducted on a single crystal wrapped with a conductive wire. Magnetotorque studies were conducted as a function of angle relative to the applied field from 0° to 112°, at discrete temperatures from 0.3 to 45 K, with field sweeps from 0 to 11 T and 11 to 45 T.

Computational Details. All electronic structure calculations were performed using the ORCA 4.0.2 package.[60,61] Multireference *ab initio* methods based on the complete active space method (CASSCF)[62] followed by N-electron valence state perturbation theory (NEVPT2)[63] were used to incorporate static and dynamic correlation. Quasi-degenerate perturbation theory (QDPT) was used to account for mixing due to spin−orbit coupling (SOC) in a second step. Scalar relativistic effects were taken into account by the second-order Douglas−Kroll−Hess Hamiltonian (DKH2). This combination of methods is widely employed in the description of magnetic properties because it allows a multiconfigurational description of the ground and low-lying excited states.[64−69] This is crucial to describe the state mixing due to SOC properly and to quantitatively examine magnetic properties. For atoms other than uranium, the def2-TZVPP basis set was used. Uranium was treated with a DKH-optimized segmented all-electron relativistically contracted basis set with TZP quality. The COSMO solvation model was included in all calculations.

CASSCF calculations were first carried out using a minimal active space CAS(2,7) corresponding to two electrons in seven 5*f* orbitals. This active space was gradually increased by including the five unoccupied 6*d* orbitals of the U^{4+} ion in a CAS(2,12) active space, and CAS(10, 16) was finally considered by adding four ligand-centered orbitals with some *d*- and *f*-character of the metal. The state-average calculations were performed for all the triplets (21 roots) and singlets (28 roots) in the minimal CAS and included the additional states when the active space increased. The CASSCF module in ORCA enables the calculation of magnetization and magnetic susceptibility curves at different fields and temperatures by differentiation of the QDPT Hamiltonian with respect to the magnetic field. For magnetic susceptibility, calculations are performed in two ways when a nonzero static magnetic field is defined, first as the second derivative of energy with respect to the magnetic field, and second as the magnetization divided by the magnetic field. The first method corresponds to the definition of magnetic susceptibility, and the second approach is widely used in the experimental determination of χT curves.

Interacting quantum atom (IQA) is an energy decomposition method that uses the quantum theory of atoms in molecules (QTAIM) to partition the total energy into intra- and interatomic terms.[70] Within the latter, the energy can be decomposed into nucleus−nucleus and electron−electron repulsion, electron−nucleus attraction, and for convenience, groups them into classical (V_{cl}) and exchange terms (V_{xc}). The classical term accounts for merely electrostatic contributions, while the exchange-correlation term accounts for quantum properties such as covalency.[71] These metrics were obtained using the AIMALL program[72] starting from the *ab*

DOI: 10.1021/acs.inorgchem.8b02800
Inorg. Chem. 2019, 58, 637−647

initio CAS(10,16) wave function for UF_8^{4-}, and are listed in Supporting Information Table S3.

RESULTS AND DISCUSSION

Structural Discussion. The unit cell parameters obtained differ significantly beyond the statistical errors in the literature. Most notably, at room temperature and 230 K, the β-angle is reduced from 121.3° to 117.2°, and the *c*-axis is shortened by over 0.5 Å. Despite this, the unit cell volume is consistent with prior results, and the same setting of the space group $C2/c$ is obtained. Attempts to force the unit cell into strict agreement with the literature from data at room temperature, 230 K, and 150 K resulted in comparable crystallographic solutions, though the 150 K data indicated a slight shrinking of the unit cell due to the temperature difference. The 117.2° unit cell at 230 K is related to the literature unit cell by a rotation around the a*c*-diagonal and are the same within SAINT indexing tolerances. As the smaller β-angle representation is preferable due to crystallographic conventions, we present that unit cell in our data here.

The UF_8^{4-} moiety is confirmed to form a distorted tetragonal antiprism with dodecahedral symmetry, as originally reported by Rosenzweig and Cromer.[27] The two antiprism faces are approximately aligned to the crystallographic ac-plane and are distorted to different degrees, as illustrated in Figure 1. The structure is held together by hydrogen−fluoride hydrogen bonds, placing the product in the category of ionic molecules. The dilute network of four ammonium cations connecting the octafluorouranate moieties results in a crystallographic density of 2.984 g/cm^3 at 230 K and 3.012 g/cm^3 at 150 K. Crystals were observed to be stable in water, oil, varnish, and static air for months at a time, although exposure to flowing air did cause the visible transformation of the product into a blue-green powder which could not be unambiguously identified.

UV−Visible−NIR Absorption Spectroscopy. Solid-state and solution-state UV−visible-NIR absorption spectroscopy confirms the tetrapositive oxidation state of uranium. There is no indication of other oxidation states present in the experimental spectra and no indication of other contributions to the absorption spectrum, as displayed in Figure 2. Strong absorption bands at 621.4, 661.0, and 1094.1 nm correspond well to the partial solution-state absorption spectra published previously.[58] Additionally, solution-phase absorption spectra observed the same peaks, with the addition of a small peak between the 621 and 661 nm absorption lines, and the general broadening of lines which obscured some details. These differences are slight, and the remarkable concordance between solution- and solid-state absorption spectra indicate that the octafluorouranate monomer is maintained in concentrated aqueous ammonium fluoride solution.

Magnetic Susceptibility Measurements. The field-dependent magnetization from 0 to 7 T is linear, indicating there is likely no change in electronic configuration over this range (Figure 3a). The field-cooled (FC) and zero-field-cooled (ZFC) susceptibility plots are presented in Figure 3b, showing near-perfect overlap of the sweeps and the presence of a flat shoulder around 50 K. A χT vs temperature plot is also presented in Figure 3c and features a linear response at temperatures below 100 K. It is worth noting that χT (Figure 3c) does not saturate by room-temperature. Since χT should saturate toward a constant value, this implies that measurements of susceptibility above room temperature would be needed to examine the saturation behavior. As $(NH_4)_4UF_8$ is known to decompose at elevated temperatures,[19−26] this was not explored.

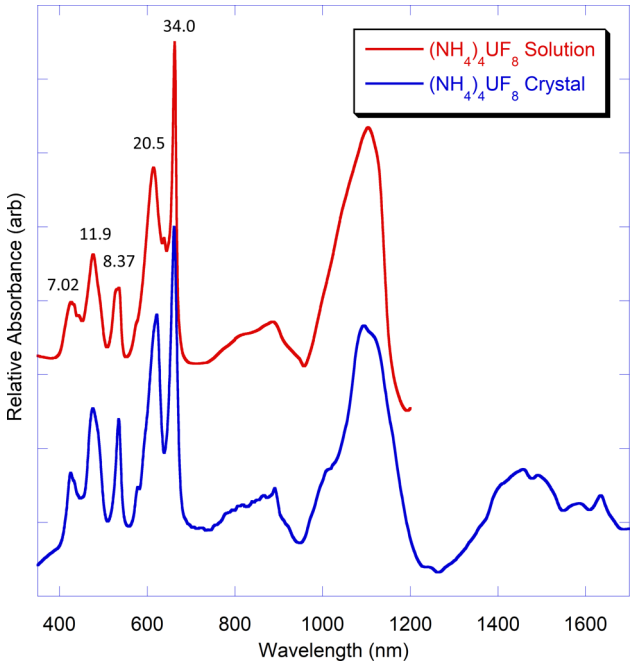

Figure 2. Solution-state (red, top) and single-crystal (blue, bottom) absorption spectra of $(NH_4)_4UF_8$. Molar absorptivity values (ε) are given in units of L·mol^{-1}·cm^{-1} for the solution-state spectrum.

Owing to the effect of crystal-electric field splitting, the Curie−Weiss formula can be considered to be an incomplete description, but it can be useful for understanding effective magnetism in the temperatures near ambient conditions. The effective magnetic moment per uranium as determined by the Curie−Weiss formula fitting the inverse susceptibility from 200 to 300 K is 3.5 μ_B, in good agreement with the theoretical value of 3.58 μ_B for an ideal f^2 Russell−Saunders system with a $^3H_4$ ground state. This result is well within the range of U^{4+} magnetization, which varies from 1.36 to 3.79 μ_B at room temperature.[73] Below 100 K, χ^{-1}(T) deviates from the tendency to increase temperature and instead begins to saturate toward approximately 150 mol/cm^3, before exhibiting a weak downturn below 20 K, indicated in Figure 4. The level susceptibility from 20 to 100 K and nonlinearity in the inverse-susceptibility plot above 200 K suggests a magnetic response which originates from a singlet ground state being split by the crystal electric field.

The increase in susceptibility below 20 K was unexpected, and experiments to preclude the possibility of magnetic ordering at these temperatures followed. As all materials in the sample holder were strongly diamagnetic and readily background-subtracted, it seemed unlikely that there would be any change in susceptibility other than from the sample, which was confirmed by re-evaluation of these instruments. Moreover, the sample was composed of three discrete and clearly identified crystals, minimizing the potential for an impure sample. It was proposed that a low-lying multiplet split in a magnetic field might crossover with the magnetic singlet and, due to reduced thermal occupation of the singlet state at low temperature, cause an increase in susceptibility. Magneto-torque measurements in the 45 T Hybrid Magnet at the National High Magnetic Field Laboratory[74] were employed to search for any indication of a nonsinglet state at a higher

DOI: 10.1021/acs.inorgchem.8b02800
Inorg. Chem. 2019, 58, 637−647

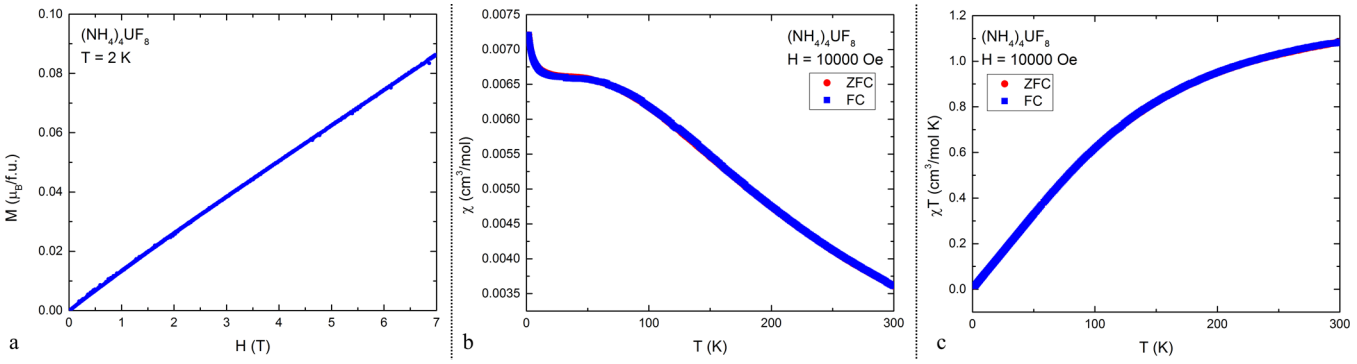

Figure 3. Visual summary of experimental magnetic response with near-perfect overlap of ZFC- and FC-susceptibilities in parts b and c.

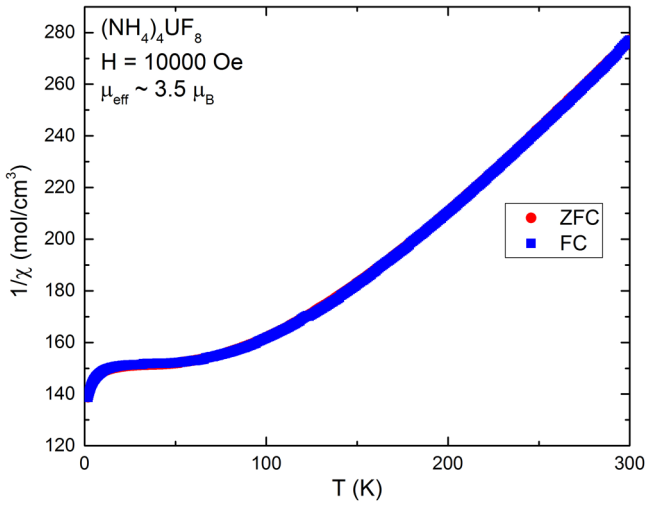

Figure 4. Inverse susceptibility vs absolute temperature from 2 to 300 K at 1 T (10 kOe). The small degree of bending observed above 100 K is due to thermally populated low-lying excited states above the ground-state singlet.

applied field, in the hopes of strongly splitting and forcing full occupancy of a paramagnetic multiplet. Figure 5 shows a summary of the magnetotorque measurements of a single crystal, with sweeps determining transitions from the angle relative to the applied field and at several temperatures. Sudden changes in magnetotorque measurements are correlated to structural, magnetic, and electronic transitions. The smooth magnetic response over this unparalleled range of applied fields suggests it is quite unlikely that $(NH_4)_4UF_8$ undergoes an electronic or structural phase transition below 50 K and determines that the low-temperature feature was due to an impurity.

There is a known tendency for the crystals of this family to give off ammonium fluoride in a vacuum or under flowing air.[26] Although precautions were taken to ensure this did not happen, it is likely that a fraction of the crystal surfaces may have converted to the magnetic $(NH_4)_2UF_6$ or other extended phases. This is supported by an observation that the dark green crystals used for magnetic measurements became "tarnished," having changed color on the surface of the crystal to a light blue-green. While both colors are common for uranium compounds, the transformation is indicative of at least partial transformation of the sample.[75] This is consistent with descriptions of $(NH_4)_2UF_6$, as well as mixed-phase product obtained by flowing air over finely powdered $(NH_4)_4UF_8$ overnight.[76]

Electronic Structure Calculations. In the molecule described here, the U^{4+} ion is surrounded in the crystal by eight F^- anions in a *quasi-D_{4d}* local symmetry with a second shell of counterions consisting of four ammonium ions. From

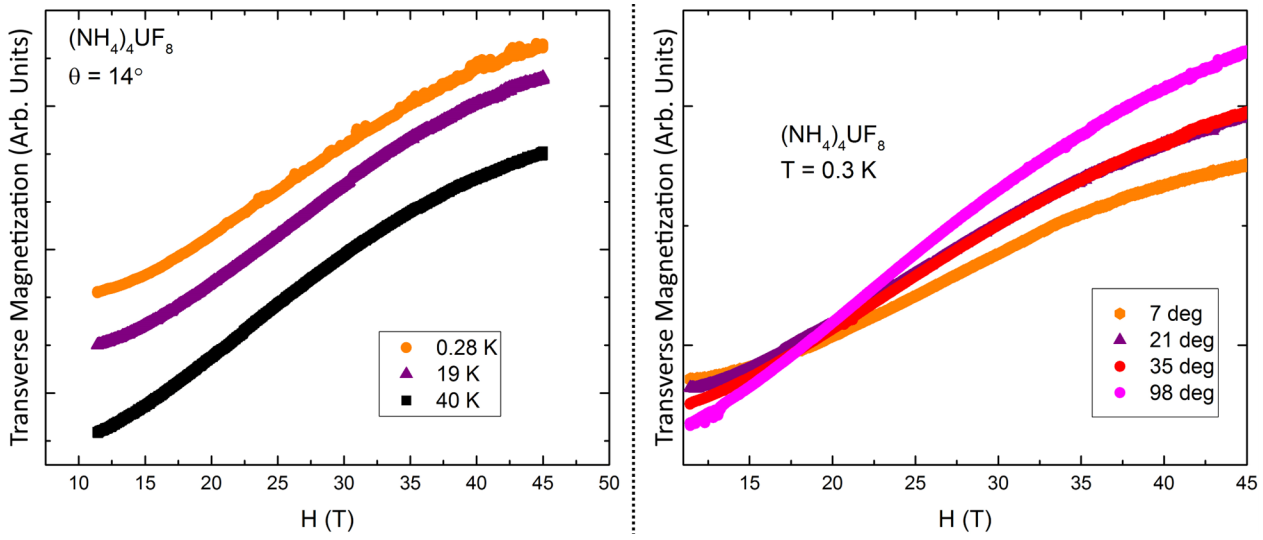

Figure 5. Summary of magnetotorque data, conducted at the National High Magnetic Field Laboratory on the 45 T Hybrid Magnet.

DOI: 10.1021/acs.inorgchem.8b02800
Inorg. Chem. 2019, 58, 637−647

the crystallographic data, it is additionally possible to consider a larger environment, where the UF_8^{4-} ion is surrounded by 16 ammonium ions. In this configuration, the structure has a C_2 axis and is referred to as the *C_2-model*. Calculations were performed for the UF_8^{4-} ion, $(NH_4)_4UF_8$ molecule, and the *C_2-model*; Figure 6 depicts the different coordination environments of the molecule and the *C_2-model*.

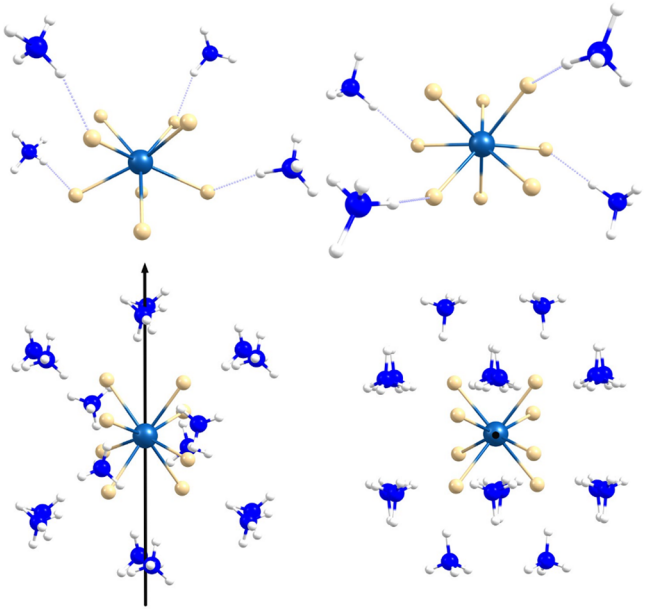

Figure 6. Molecular models for $(NH_4)_4UF_8$ obtained from crystallographic data. Views which are perpendicular to and through the *quasi*-C_4 (C_2) axis are presented on the left and right. Two models which considered different arrangements of counterions are presented, with four ammonium ions in the top representation, and 16 ammonium ions in the bottom representation.

According to Hund's rule, the spin-free ground term of the U^{4+} ion is ^3H, which is split by spin−orbit interaction into ^3H_J (J = 4, 5, 6) terms, with $^3H_4$ as the ground state. The surrounding atoms apply a specific symmetry-dependent crystal field which again split the ground term. If a D_{4d} symmetry is assumed, three singly- (A_1, B_1, B_2) and doubly degenerate states (E_1, E_2, E_3) are formed. In the case of UF_8^{4-}, this degeneracy is lifted by a break in the symmetry of the structure, resulting in nine separate states. This can be seen in Supporting Information Figure S1, in an electronic states diagram from ab initio calculations of UF_8^{4-}. The combined crystal-field and spin−orbit interaction also mixes $^3H_4$ with excited J = 4 levels, with the dominant excited-state contribution from the $^1G_4$ state, constituting around 10% of the ground state. This multireference ground state is a consistent result, no matter the size of the active space or the considered molecular model (see Table 2 and Supporting Information Table S1), and changes in the relative energies of the states are almost negligible when the considered active space is augmented.

On the other hand, the introduction of dynamic correlation via NEVPT2 produces a slight destabilization of the excited states, but the metal−ligand interaction by orbital mixing does not increase (see Table 3 and Supporting Information Table S2). Examination of the U−F bonds by IQA energy decomposition determined that the average interaction between the uranium and fluorine ions is 91% electrostatic and 9% due to exchange correlation. It is this exchange correlation which considers covalency, so the bond here is properly considered a predominantly ionic interaction. This determination can be reinforced from the analysis of the optimized molecular orbitals which show almost negligible metal contribution in the ligand-centered orbitals included in the active space. Supporting Information Table S3 provides IQA energy decomposition values for the UF_8^{4-} ion. Ultimately, the occupation of the 5*f* orbitals did not vary much, regardless of the chosen active space, as illustrated in Figure 7. Calculated absorption spectra may therefore consider the wave functions of the simpler UF_8^{4-} ion.

As excitations within the UV−visible regime correspond to electronic transitions, they are of primary interest for ensuring that the underlying electronic structure theory corresponds well to physical observables. When the wave functions derived from the CAS(2,7) active space were employed without spin−orbit corrections (SOC), poor absorption spectra which did approximate the absorption bands seen around 420 and 1600 nm were obtained, though there was little qualitative resemblance to the transitions observed in the experimental spectra. The addition of SOC yielded spectra which approximately modeled the shape of the absorption spectra, but absorption peaks were still shifted to higher energy, by 300−400 nm in most cases. Further consideration of NEVPT2 resulted in theoretical spectra which matched the experimental results in shape and relative intensity to a remarkable degree. There was little difference between varying levels of CAS. Figures illustrating these methods are found in the Supporting Information, as is a simulated absorption spectrum derived from Time-Dependent Density Functional Theory (TD-DFT),

Table 2. Relative Calculated Energies (in cm^{-1}) of the Low Energy States of Optimized UF_8^{4-} and $(NH_4)_4UF_8$ from SO-CASSCF Calculations

UF_8^{4-}				$(NH_4)_4UF_8$			
CAS(2,7)	% $^3H_4$	CAS(10,16)	% $^3H_4$	CAS(2,7)	% $^3H_4$	CAS(10,16)	% $^3H_4$
0.0	93.3	0.0	93.3	0.0	93.1	0.0	93.1
143.6	92.3	143.5	92.2	173.2	91.8	173.8	91.8
324.9	91.2	323.6	91.2	342.4	91.2	341.3	91.2
379.8	90.7	374.6	90.5	471.5	90.0	471.3	90.0
648.0	92.9	641.8	93.1	725.2	92.3	723.9	96.1
1039.3	91.5	1036.6	91.6	1073.6	91.7	1073.5	91.7
1203.6	90.9	1200.4	90.7	1245.6	91.7	1246.1	91.8
1404.3	90.5	1401.2	91.3	1414.7	91.7	1415.0	91.7
1488.7	91.2	1485.5	91.0	1498.8	91.5	1499.3	91.5

DOI: 10.1021/acs.inorgchem.8b02800
Inorg. Chem. 2019, 58, 637−647

Table 3. Relative Calculated Energies (in cm^{-1}) of the Low Energy States of Optimized UF_8^{4-} and $(NH_4)_4UF_8$ from SO-NEVPT2 Calculations

UF_8^{4-}				$(NH_4)_4UF_8$			
CAS(2,7)	% $^3H_4$	CAS(10,16)	% $^3H_4$	CAS(2,7)	% $^3H_4$	CAS(10,16)	% $^3H_4$
0.0	92.6	0.0	92.6	0.0	92.5	0.0	92.5
164.5	91.4	162.1	91.4	193.1	91.2	193.8	91.2
335.9	90.3	328.6	90.2	358.3	90.7	354.1	90.6
401.6	89.7	382.5	89.6	487.1	89.6	482.4	89.5
657.5	92.4	636.3	92.6	723.4	91.8	717.4	91.7
1066.2	91.0	1040.3	90.6	1084.9	91.0	1080.1	90.9
1211.1	90.1	1184.3	89.7	1246.3	90.2	1242.3	89.9
1457.4	90.8	1477.4	90.3	1467.3	91.1	1474.5	90.8
1528.0	90.5	1546.7	90.1	1532.6	90.8	1539.4	90.8

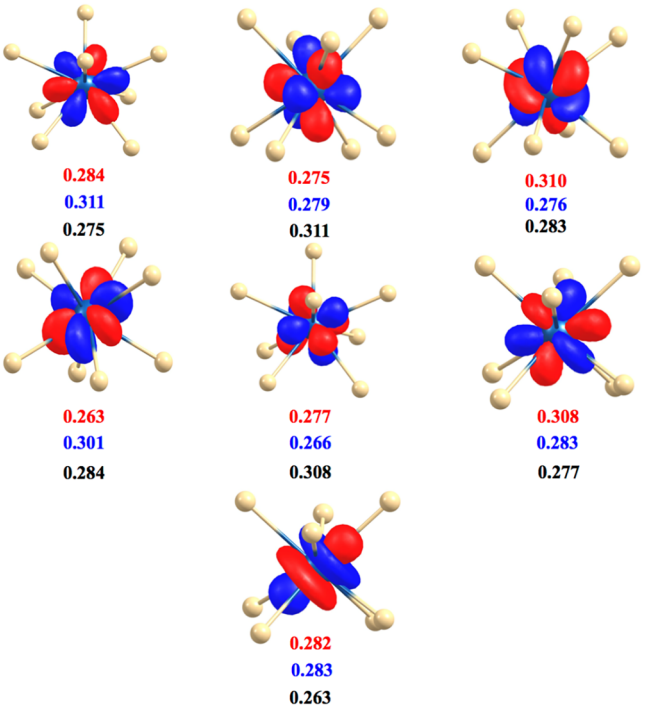

Figure 7. Occupation numbers of the 5*f* orbitals in the three different active spaces studied. CAS(2,7), CAS(2,12), and CAS(10,16) results are presented in red, blue, and black, respectively.

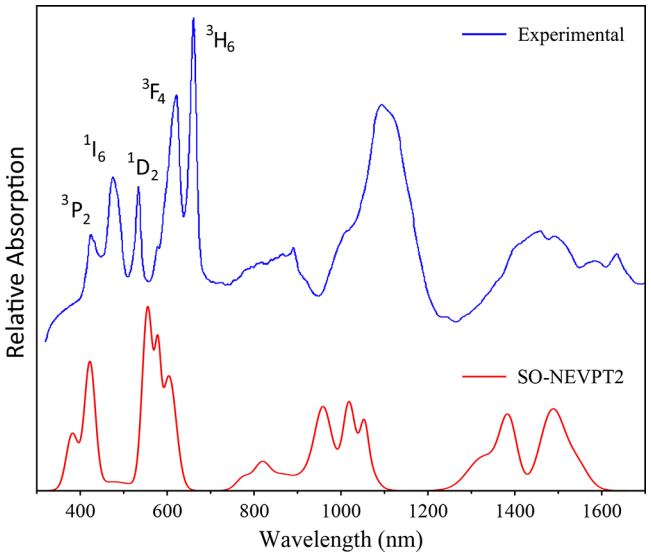

Figure 8. Comparison between the experimental single-crystal absorption spectrum (blue, top) and the calculated absorption spectrum (red, bottom). Transitions from the $^3H_4$ ground state are indicated in black.

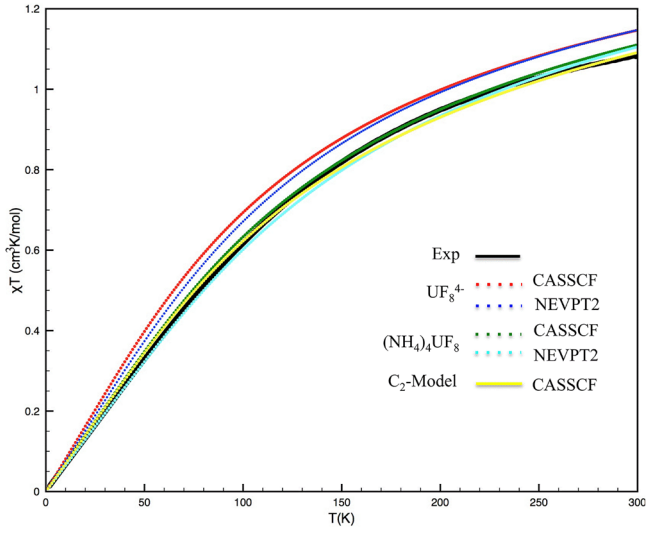

Figure 9. Calculated magnetic susceptibility χT ($cm^3 \cdot K \cdot mol^{-1}$) for the three studied models at different levels of theory presented with the experimental results. The active space CAS(10,16) was used except for the *C_2-model* which was treated with the minimal active space CAS(2,7).

which only featured soft-UV ligand-to-metal charge transfer bands. The primary differences observed between the CASSCF results and the experimental absorption spectrum is the shape of the absorption band experimentally absorbed at 1094 nm, the theoretical observation of a triplet in the 600 nm region (rather than a 500 nm singlet and a ~630 nm doublet), and a persistent underestimation of peak energy by ~50 nm. A visual comparison between these theoretical and experimental results is given in Figure 8, as are five electronic transitions visible from 400 to 700 nm. It is this excellent replication of the absorption spectra which enables a candid look at the low-energy excited states of this product and provides confidence in the model for the treatment of magnetic properties.

Theoretical Assessment of Magnetic Features. The variable-temperature magnetic susceptibility curves calculated for UF_8^{4-} are in good agreement with the experimental magnetization above 25 K. At low temperatures, χT increases linearly with T (see Figure 9), meaning that χ is constant, and in this temperature range, the system is in a temperature-

DOI: 10.1021/acs.inorgchem.8b02800
Inorg. Chem. 2019, 58, 637−647

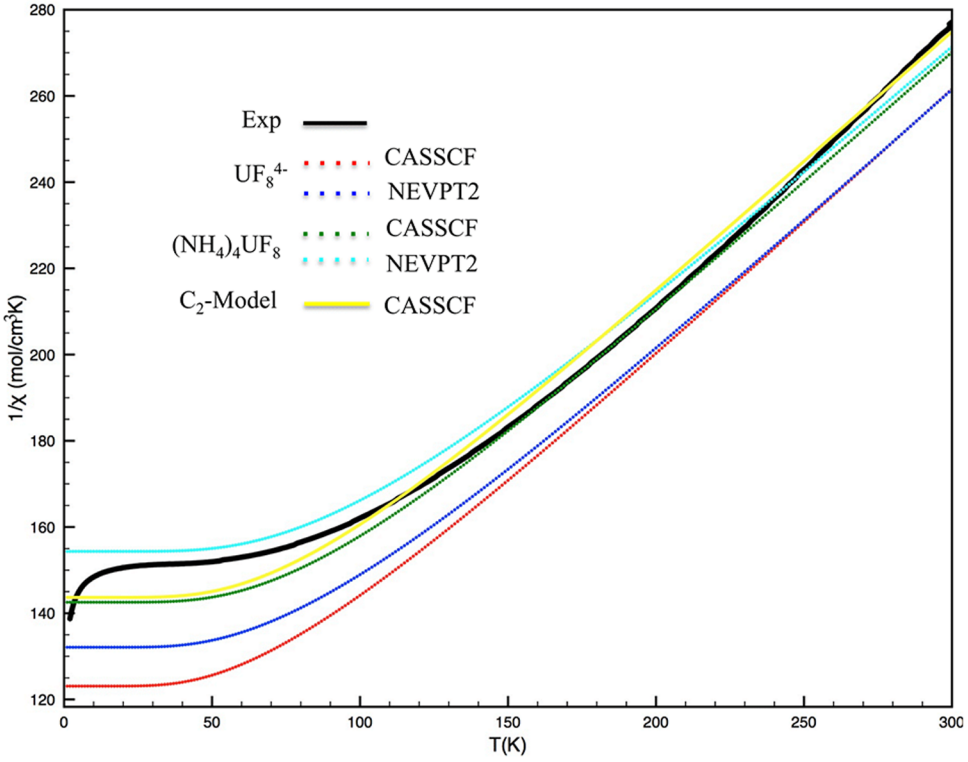

Figure 10. Calculated inverse magnetic susceptibility as a function of temperature for the three proposed models at different levels of theory, presented as overlapping with the experimental results. The active space CAS(10,16) was used except for the *C_2-model* which was treated with the minimal active space CAS(2,7).

independent paramagnetic regime. A crystal field analysis determined that the orbital singlet $m_J = 0$ state dominates the $^3H_4$ ground term, with excited state contribution from thermal population of $m_J = \pm1$ and ±4 states at higher temperatures. This calculated sequence of levels agrees with the temperature-dependence of the paramagnetic susceptibility near ambient conditions. As this system features a nonmagnetic ground state at low temperatures, only the coupling between ground and excited states (via magnetic dipole moment transition) contributes to the susceptibility.

Above 50 K, the susceptibility becomes temperature-dependent, and the common proportional relation of χ^{-1} vs T is observed (Figure 10), though there is no bending visible in the modeled susceptibility. The excellent agreement with the experimental susceptibility curves confirms that the selected models and active spaces successfully treat the molecular electronic states. It does appear that the inclusion of the counterions from the crystallographic data improves the accuracy of the results, as the full molecule CASSCF, NEVPT2, and the *C_2-model* visually matches the observed susceptibility of 1/150 cm^3/mol. The results for the $(NH_4)_4UF_8$ model with the larger active space produce almost the same results that the minimal active space *C_2-model* obtained. The theoretical magnetic moment was 3.68 μ_B for the isolated ion of UF_8^{4-}, and 3.66 μ_B for $(NH_4)_4UF_8$, in good agreement with the experimental moment of 3.5 μ_B. None of these calculations were able to provide a theoretical basis for a changing low-temperature susceptibility, and any low-lying multiplet states were not determined to crossover the singlet state at the fields examined experimentally or theoretically. Resultingly, $(NH_4)_4UF_8$ should be considered to have a nonmagnetic ground state, with paramagnetic excited states thermally populated above 100 K.

CONCLUSION

The structure of $(NH_4)_4UF_8$ has been revisited with advanced characterization tools, and two new high-resolution structures have been obtained. The solution- and solid-state absorption features of the uranium(IV) fluoride species have been compared and agree well with each other. Magnetic susceptibility measurements show the presence of a strongly favored singlet state at low-temperature, that was further supported by high-field magnetotorque measurements up to 45 T. Theoretical treatment of the molecule has examined physical, electronic, and magnetic structure and provides great insight into the fundamental features of uranium(IV) compounds and $5f^2$ systems more generally.

ASSOCIATED CONTENT

Supporting Information

The Supporting Information is available free of charge on the ACS Publications website at DOI: 10.1021/acs.inorgchem.8b02800.

Additional tables of computed low-energy optimized states and IQA decomposition, an electronic states diagram, comparisons between theoretical and experimental UV−visible absorption spectra and magnetic response at different levels of theory, atomic coordinates, structural details, and refinement information for the published crystal structure. (PDF)

DOI: 10.1021/acs.inorgchem.8b02800
Inorg. Chem. 2019, 58, 637−647

Accession Codes

CCDC 1868290 and 1879530 contain the supplementary crystallographic data for this paper. These data can be obtained free of charge via www.ccdc.cam.ac.uk/data_request/cif, or by emailing data_request@ccdc.cam.ac.uk, or by contacting The Cambridge Crystallographic Data Centre, 12 Union Road, Cambridge CB2 1EZ, UK; fax: +44 1223 336033.

AUTHOR INFORMATION

Corresponding Authors

*E-mail: albrecht-schmitt@chem.fsu.edu.
*E-mail: graf@magnet.fsu.edu.

ORCID

Alexander T. Chemey: 0000-0002-0679-7845
Cristian Celis-Barros: 0000-0002-4685-5229
Kevin Huang: 0000-0003-2718-2214
Joseph M. Sperling: 0000-0003-1916-5633
Cory J. Windorff: 0000-0002-5208-9129
Ryan E. Baumbach: 0000-0002-6314-3629
David E. Graf: 0000-0001-6195-0462
Dayán Páez-Hernández: 0000-0003-2747-9982
David E. Hobart: 0000-0001-8850-469X
Thomas E. Albrecht-Schmitt: 0000-0002-2989-3311

Notes

The authors declare no competing financial interest.

ACKNOWLEDGMENTS

This research was supported by the Center for Actinide Science and Technology (CAST), an Energy Frontier Research Center (EFRC) funded by the US Department of Energy (DOE), Office of Science, Basic Energy Sciences (BES), under Award Number DE-SC0016568. A portion of this work was performed at the National High Magnetic Field Laboratory, which is supported by the National Science Foundation Cooperative Agreement No. DMR-1157490 and No. DMR-1644779 and the State of Florida.

REFERENCES

(1) Cunningham, B. B.; Werner, L. B. The First Isolation of Plutonium. *J. Am. Chem. Soc.* **1949**, *71*, 1521−1528.
(2) Morel, B.; Duperret, B. Uranium and Fluorine Cycles in the Nuclear Industry. *J. Fluorine Chem.* **2009**, *130*, 7−10.
(3) McNamara, B.; Scheele, R.; Kozelisky, A.; Edwards, M. Thermal Reactions of Uranium Metal, UO_2, U_3O_8, UF_4, and UO_2F_2 with NF_3 to Produce UF_6. *J. Nucl. Mater.* **2009**, *394*, 166−173.
(4) Weinstock, B.; Crist, R. The Vapor Pressure of Uranium Hexafluoride. *J. Chem. Phys.* **1948**, *16*, 436−441.
(5) Rosenthal, M. W.; Kasten, P. R.; Briggs, R. B. Molten-Salt Reactors—History, Status, and Potential. *Nucl. Appl. Technol.* **1970**, *8*, 107−117.
(6) Heuer, D.; Merle-Lucotte, E.; Allibert, M.; Brovchenko, M.; Ghetta, V.; Rubiolo, P. Towards the Thorium Fuel Cycle with Molten Salt Fast Reactors. *Ann. Nucl. Energy* **2014**, *64*, 421−429.
(7) Serp, J.; Allibert, M.; Beneš, O.; Delpech, S.; Feynberg, O.; Ghetta, V.; Heuer, D.; Holcomb, D.; Ignatiev, V.; Kloosterman, J.; Luzzi, L.; Merle-Lucotte, E.; Uhlir, J.; Yoshioka, R.; Zhimin, D. The Molten Salt Reactor (MSR) in Generation IV: Overview and Perspectives. *Prog. Nucl. Energy* **2014**, *77*, 308−319.
(8) LeBlanc, D. Molten Salt Reactors: A New Beginning for an Old Idea. *Nucl. Eng. Des.* **2010**, *240*, 1644−1656.
(9) Ponomarev, L.; Seregin, M.; Parshin, A.; Mel'nikov, S.; Mikhalichenko, A.; Zagorets, L.; Manuilov, R.; Rzheutskii, A. Fuel Salt for the Molten-Salt Reactor. *At. Energy* **2013**, *115*, 5−10.
(10) Mathieu, L.; Heuer, D.; Merle-Lucotte, E.; Brissot, R.; Brun, L. C.; Liatard, E.; Loiseaux, J.-M.; Méplan, O.; Nuttin, A.; Lecarpentier, D. Possible Configurations for the Thorium Molten Salt Reactor and Advantages of the Fast Nonmoderated Version. *Nucl. Sci. Eng.* **2009**, *161*, 78−89.
(11) Mathieu, L.; Heuer, D.; Brissot, R.; Garzenne, C.; LeBrun, C.; Lecarpentier, D.; Liatard, E.; Loiseaux, J.-M.; Meplan, O.; Merle-Lucotte, E.; Nuttin, A.; Walle, E.; Wilson, J. The Thorium Molten Salt Reactor: Moving on from the MSBR. *Prog. Nucl. Energy* **2006**, *48*, 664−679.
(12) Delpech, S.; Merle-Lucotte, E.; Heuer, D.; Allibert, M.; Ghetta, V.; Le-Brun, C.; Doligez, X.; Picard, G. Reactor Physic and Reprocessing Scheme for Innovative Molten Salt Reactor System. *J. Fluorine Chem.* **2009**, *130*, 11−17.
(13) Yu, C.; Li, X.; Cai, X.; Zou, C.; Ma, Y.; Wu, J.; Han, J.; Chen, J. Minor Actinide Incineration and Th-U Breeding in a Small FLiNaK Molten Salt Fast Reactor. *Ann. Nucl. Energy* **2017**, *99*, 335−344.
(14) Cary, S. K.; Boland, K. S.; Cross, J. N.; Kozimor, S. A.; Scott, B. L. Advances in Containment Methods and Plutonium Recovery Strategies That Led to the Structural Characterization of Plutonium-(IV) Tetrachloride Tris-Diphenylsulfoxide, $PuCl_4(OSPh_2)_3$. *Polyhedron* **2017**, *126*, 220−226.
(15) Cary, S. K.; Su, J.; Galley, S. S.; Albrecht-Schmitt, T. E.; Batista, E. R.; Ferrier, M. G.; Kozimor, S. A.; Mocko, V.; Scott, B. L.; Alstine, C. E.; White, F. D.; Yang, P. A Series of Dithiocarbamates for Americium, Curium, and Californium. *Dalton Transactions* **2018**, *47*, 14452−14461.
(16) Penneman, R. A.; Keenan, T. K.; Asprey, L. B. Tetra- and Pentavalent Actinide Fluoride Complexes. In *Lanthanide/Actinide Chemistry*; Fields, P. R., Moeller, T., Ed.; American Chemical Society: Washington, DC, 1967; pp 248−255.
(17) Penneman, R. A.; Ryan, R. R.; Rosenzweig, A. The Novel Structure of $(NH_4)_4ThF_8$. *Chem. Commun.* **1968**, 990−991.
(18) Ryan, R. R.; Penneman, R. A.; Rosenzweig, A. The Crystal Structure of Ammonium Thorium (IV) Octafluoride, $(NH_4)_4ThF_8$. *Acta Crystallogr., Sect. B: Struct. Crystallogr. Cryst. Chem.* **1969**, *25*, 1958−1962.
(19) Yeamans, C. B.; Silva, G. W.; Cerefice, G. S.; Czerwinski, K. R.; Hartmann, T.; Burrell, A. K.; Sattelberger, A. P. Oxidative Ammonolysis of Uranium(IV) Fluorides to Uranium(VI) Nitride. *J. Nucl. Mater.* **2008**, *374*, 75−78.
(20) Poineau, F.; Silva, C.; Yeamans, C. B.; Cerefice, G. S.; Sattelberger, A. P.; Czerwinski, K. R. Structural Study of the Ammonium Octafluoroneptunate, $[NH_4]_4NpF_8$. *Inorg. Chim. Acta* **2016**, *448*, 93−96.
(21) Silva, C. G.; Weck, P. F.; Kim, E.; Yeamans, C. B.; Cerefice, G. S.; Sattelberger, A. P.; Czerwinski, K. R. Crystal and Electronic Structures of Neptunium Nitrides Synthesized Using a Fluoride Route. *J. Am. Chem. Soc.* **2012**, *134*, 3111−3119.
(22) Wani, B. N.; Patwe, S. J.; Rao, U. R. K.; Venkateswarlu, K. S. Fluorination of Oxides of Uranium and Thorium by Ammonium Hydrogenfluoride. *J. Fluorine Chem.* **1989**, *44*, 177−185.
(23) Claux, B.; Beneš, O.; Capelli, E.; Souček, P.; Meier, R. On the Fluorination of Plutonium Dioxide by Ammonium Hydrogen Fluoride. *J. Fluorine Chem.* **2016**, *183*, 10−13.
(24) Tolley, W. *The Preparation of Plutonium (IV) Ammonium Fluoride and Its Decomposition to Plutonium Tetrafluoride for Subsequent Reduction to Metal*; HW-31211; Hanford Atomic Products Operation: Richland, WA, 1954.
(25) Yahata, T.; Muromura, T.; Ouchi, K.; Naito, K. A Study of Ammonium Plutonium(IV) Fluorides—II: The Thermal Decomposition of Ammonium Plutonium(IV) Fluorides, Ammonium Cerium(IV) Fluoride and Ammonium Uranium(IV) Fluoride. *J. Inorg. Nucl. Chem.* **1971**, *33*, 3339−3343.
(26) Benz, R.; Douglass, R. M.; Kruse, F. H.; Penneman, R. A. Preparation and Properties of Several Ammonium Uranium (IV) and Ammonium Plutonium (IV) Fluorides. *Inorg. Chem.* **1963**, *2*, 799−803.

DOI: 10.1021/acs.inorgchem.8b02800
Inorg. Chem. 2019, 58, 637−647

(27) Rosenzweig, A.; Cromer, D. The Crystal Structure of $(NH_4)_4UF_8$. *Acta Crystallogr., Sect. B: Struct. Crystallogr. Cryst. Chem.* **1970**, *26*, 38−44.
(28) Ryan, R. R.; Larson, A. C.; Kruse, F. H. Crystal Structure of Ammonium Hexafluorocerate (IV), $(NH_4)_2CeF_6$. *Inorg. Chem.* **1969**, *8*, 33−36.
(29) Hellenbrandt, M. The Inorganic Crystal Structure Database (ICSD)—Present and Future. *Crystallogr. Rev.* **2004**, *10*, 17−22.
(30) Zachariasen, W. Crystal Chemical Studies of the 5*f*-Series of Elements. XXII. The Crystal Structure of K_3UF_7. *Acta Crystallogr.* **1954**, *7*, 792−794.
(31) Zachariasen, W. Crystal Chemical Studies of the 5*f*-series of Elements. XXIII. On the Crystal Chemistry of Uranyl Compounds and of Related Compounds of Transuranic Elements. *Acta Crystallogr.* **1954**, *7*, 795−799.
(32) Zachariasen, W. Crystal Chemical Studies of the 5*f*-Series of Elements. XII. New Compounds Representing Known Structure Types. *Acta Crystallogr.* **1949**, *2*, 388−390.
(33) Brunton, G. The Crystal Structure of KU_2F_9. *Acta Crystallogr., Sect. B: Struct. Crystallogr. Cryst. Chem.* **1969**, *25*, 1919−1921.
(34) Yeon, J.; Smith, M. D.; Tapp, J.; Möller, A.; zur Loye, H.-C. Mild Hydrothermal Crystal Growth, Structure, and Magnetic Properties of Ternary U(IV) Containing Fluorides: $LiUF_5$, KU_2F_9, $K_7U_6F_{31}$, $RbUF_5$, RbU_2F_9, and RbU_3F_{13}. *Inorg. Chem.* **2014**, *53*, 6289−6298.
(35) Almond, P. M.; Deakin, L.; Mar, A.; Albrecht-Schmitt, T. E. Hydrothermal Syntheses, Structures, and Magnetic Properties of the U(IV) Fluorides $(C_5H_{14}N_2)_2U_2F_{12}\cdot 5H_2O$ and $(NH_4)_7U_6F_{31}$. *J. Solid State Chem.* **2001**, *158*, 87−93.
(36) Brunton, G. The Crystal Structure of Li_4UF_8. *J. Inorg. Nucl. Chem.* **1967**, *29*, 1631−1636.
(37) Chebotarev, N.; Beznosikova, A. The Structure of $CaUF_6$. *Soviet Atomic Energy* **1968**, *25*, 1119−1122.
(38) Abazli, H.; Cousson, A.; Tabuteau, A.; Pagès, M.; Gasperin, M. Fluorure d'Ammonium et d'Uranium(IV): $NH_4U_3F_{13}$. *Acta Crystallogr., Sect. B: Struct. Crystallogr. Cryst. Chem.* **1980**, *36*, 2765−2766.
(39) Brunton, G. The Crystal Structure of $LiUF_5$. *Acta Crystallogr.* **1966**, *21*, 814−817.
(40) Avignant, D.; Mansouri, I.; Sabatier, R.; Cousseins, J.-C.; Chevalier, R. Structure Du Fluorure de Thallium(I) et d'Uranium-(IV). *Acta Crystallogr., Sect. B: Struct. Crystallogr. Cryst. Chem.* **1980**, *36*, 664−666.
(41) Védrine, A.; Baraduc, L.; Cousseins, J.-C. Sur Une Nouvelle Famille de Composes $M^{II}M^{IV}Li_2F_8$ de Structure Apparentee a Celle de La Scheelite. *Mater. Res. Bull.* **1973**, *8*, 581−587.
(42) Védrine, A.; Trottier, D.; Cousseins, J.-C.; Chevalier, R. Crystal Structure of Li_2CaUF_8. *Mater. Res. Bull.* **1979**, *14*, 583−587.
(43) Penneman, R.; Ryan, R.; Rosenzweig, A. Preparation and Single-Crystal Structure of β-NH_4UF_5, Ammonium Pentafluoruranate(IV). *Acta Crystallogr., Sect. B: Struct. Crystallogr. Cryst. Chem.* **1974**, *30*, 1966−1970.
(44) Felder, J.; Yeon, J.; Smith, M.; zur Loye, H.-C. Application of a Mild Hydrothermal Method to the Synthesis of Mixed Transition-Metal(II)/Uranium(IV) Fluorides. *Inorg. Chem. Front.* **2017**, *4*, 368−377.
(45) Felder, J. B.; Yeon, J.; Smith, M. D.; zur Loye, H.-C. Compositional and Structural Versatility in an Unusual Family of Anti-Perovskite Fluorides: $[Cu(H_2O)_4]_3[(MF_6)(M'F_6)]$. *Inorg. Chem.* **2016**, *55*, 7167−7175.
(46) Yeon, J.; Smith, M. D.; Tapp, J.; Möller, A.; zur Loye, H.-C. Mild Hydrothermal Crystal Growth of New Uranium(IV) Fluorides, $Na_{3.13}Mg_{1.43}U_6F_{30}$ and $Na_{2.50}Mn_{1.75}U_6F_{30}$: Structures, Optical and Magnetic Properties. *J. Solid State Chem.* **2016**, *236*, 83−88.
(47) Yeon, J.; Smith, M. D.; Morrison, G.; zur Loye, H.-C. Trivalent Cation-Controlled Phase Space of New U(IV) Fluorides, $Na_3MU_6F_{30}$ (M = Al^{3+}, Ga^{3+}, Ti^{3+}, V^{3+}, Cr^{3+}, Fe^{3+}): Magnetic Properties. *Inorg. Chem.* **2015**, *54*, 2058−2066.
(48) Yeon, J.; Smith, M. D.; Tapp, J.; Möller, A.; zur Loye, H.-C. Application of a Mild Hydrothermal Approach Containing an in Situ Reduction Step to the Growth of Single Crystals of the Quaternary U(IV)-Containing Fluorides $Na_4MU_6F_{30}$(M = Mn^{2+}, Co^{2+}, Ni^{2+}, Cu^{2+}, and Zn^{2+}) Crystal Growth, Structures, and Magnetic Properties. *J. Am. Chem. Soc.* **2014**, *136*, 3955−3963.
(49) Olchowka, J.; Volkringer, C.; Henry, N.; Loiseau, T. Crystal Structures of Tetravalent Uranium Fluorides Obtained in the Presence of Hydrazine from Uranyl Source. *J. Fluorine Chem.* **2014**, *159*, 1−7, 1
(50) Schmidt, R.; Müller, B. Einkristalluntersuchungen an $Cs[AuF_4]$, $Cs[Au_2F_7]$ und $U_2F_7[AuF_4]$. *Z. Anorg. Allg. Chem.* **2004**, *630*, 2393−2397.
(51) Brunton, G. Refinement of the Crystal Structure of β_1-K_2UF_6. *Acta Crystallogr., Sect. B: Struct. Crystallogr. Cryst. Chem.* **1969**, *25*, 2163−2164.
(52) Brunton, G. The Crystal Structure of CsU_6F_{25}. *Acta Crystallogr., Sect. B: Struct. Crystallogr. Cryst. Chem.* **1971**, *27*, 245−247.
(53) Cousson, A.; Tabuteau, A.; Pagès, M.; Gasperin, M. Disodium Uranium(IV) Fluoride. *Acta Crystallogr., Sect. B: Struct. Crystallogr. Cryst. Chem.* **1979**, *35*, 1198−1200.
(54) Rosenzweig, A.; Ryan, R. R.; Cromer, D. T. The Crystal Structure of Cesium Nonafluorodiuranate(IV), CsU_2F_9. *Acta Crystallogr., Sect. B: Struct. Crystallogr. Cryst. Chem.* **1973**, *29*, 460−462.
(55) Kruse, F. H. The Crystal Structure of Rb_2UF_6. *J. Inorg. Nucl. Chem.* **1971**, *33*, 1625−1627.
(56) Chemey, A. T.; Sperling, J. M.; Albrecht-Schmitt, T. E. Expanding Pentafluorouranates: Hydrothermal Synthesis and Characterization of β-$NaUF_5$ and β-$NaUF_5\cdot H_2O$. *RSC Adv.* **2018**, *8*, 28642−28648.
(57) Taylor, J.; Wilson, P. Neutron and X-ray Powder Diffraction Studies of the Structure of Uranium Hexachloride. *Acta Crystallogr., Sect. B: Struct. Crystallogr. Cryst. Chem.* **1974**, *30*, 1481−1484.
(58) Penneman, R. A.; Kruse, F. H.; George, R. S.; Coleman, J. S. Studies of the Ammonium Fluoride-Uranium Tetrafluoride-Water System. Properties of $(NH_4)_4UF_8$, $(NH_4)_2UF_6$, $7NH_4F\cdot 6UF_4$, and of U(IV) in Aqueous NH_4F. *Inorg. Chem.* **1964**, *3*, 309−315.
(59) Liengme, B. V.. Using Solver. In *A Guide to Microsoft Excel 2013 for Scientists and Engineers*; Academic Press: Cambridge, MA, 2016; pp 247−271.
(60) Neese, F. The ORCA Program System. *WIREs Computational Molecular Science* **2012**, *2*, 73−78.
(61) Neese, F. Software Update: The ORCA Program System, Version 4.0. *WIREs Computational Molecular Science* **2018**, *8*, 1−6.
(62) Siegbahn, P. E. M.; Almlöf, J.; Heiberg, A.; Roos, B. O. The Complete Active Space SCF (CASSCF) Method in a Newton−Raphson Formulation with Application to the HNO Molecule. *J. Chem. Phys.* **1981**, *74*, 2384−2396.
(63) Angeli, C.; Cimiraglia, R.; Malrieu, J.-P. N-Electron Valence State Perturbation Theory: A Spinless Formulation and an Efficient Implementation of the Strongly Contracted and of the Partially Contracted Variants. *J. Chem. Phys.* **2002**, *117*, 9138−9153.
(64) Solis-Céspedes, E.; Páez-Hernández, D. Modeling the Electronic States and Magnetic Properties Derived from the f^1 Configuration in Lanthanocene and Actinocene Compounds. *Dalton Transactions* **2017**, *46* (14), 4834−4843.
(65) Páez-Hernández, D.; Murillo-López, J.; Arratia-Pérez, R. Optical and Magnetic Properties of the Complex Bis-(Dicyclooctatetraenyl)Diuranium. A Theoretical View. *Organometallics* **2012**, *31*, 6297−6304.
(66) Gendron, F.; Páez-Hernández, D.; Notter, F.-P.; Pritchard, B.; Bolvin, H.; Autschbach, J. Magnetic Properties and Electronic Structure of Neptunyl(VI) Complexes: Wavefunctions, Orbitals, and Crystal-Field Models. *Chem. - Eur. J.* **2014**, *20*, 7994−8011.
(67) Gendron, F.; Autschbach, J. Ligand NMR Chemical Shift Calculations for Paramagnetic Metal Complexes: $5f^1$ vs $5f^2$ Actinides. *J. Chem. Theory Comput.* **2016**, *12*, 5309−5321.
(68) Spivak, M.; Vogiatzis, K. D.; Cramer, C. J.; de Graaf, C.; Gagliardi, L. Quantum Chemical Characterization of Single Molecule Magnets Based on Uranium. *J. Phys. Chem. A* **2017**, *121*, 1726−1733.

DOI: 10.1021/acs.inorgchem.8b02800
Inorg. Chem. 2019, 58, 637−647

(69) Autschbach, J. Orbitals for Analyzing Bonding and Magnetism of Heavy-Metal Complexes. *Comments Inorg. Chem.* **2016**, *36*, 215−244.
(70) Blanco, M. A.; Pendás, A. M.; Francisco, E. Interacting Quantum Atoms: A correlated Energy Decomposition Scheme Based on the Quantum Theory of Atoms in Molecules. *J. Chem. Theory Comput.* **2005**, *1*, 1096−1109.
(71) Du, J.; Sun, J.; Jiang, G. Exploring the Interaction Natures in Plutonyl (VI) Complexes with Topological Analyses of Electron Density. *Int. J. Mol. Sci.* **2016**, *17*, 414−426.
(72) Keith, T. A. *AIMAll (Version 17.11.14)*; https://aim.tkgristmill.com, 2017.
(73) Kindra, D. R.; Evans, W. J. Magnetic Susceptibility of Uranium Complexes. *Chem. Rev.* **2014**, *114*, 8865−8882.
(74) Chen, K.; Lian, X.; Lai, Y.; Aryal, N.; Chiu, Y.; Lan, W.; Graf, D.; Manousakis, E.; Baumbach, R. E.; Balicas, L. Bulk Fermi Surfaces of the Dirac Type-II Semimetallic Candidates MAl_3 (Where M = V, Nb, and Ta). *Phys. Rev. Lett.* **2018**, *120*, 206401.
(75) Rudel, S. S.; Pietzonka, C.; Hoelzel, M.; Kraus, F. $[UCl_4(HCN)_4]$ − A Hydrogen Cyanide Complex of Uranium Tetrachloride. *Chem. Commun.* **2018**, *54*, 1241−1244.
(76) Kiselev, Y. M.; Zelentsov, V. V.; Fal'kengof, A. T. Thermal and Magnetic Properties of Uranium(IV) Ammonium Fluorocomplexes. *Koordinatsionnaya Khimiya* **1978**, *4*, 725−728.

DOI: 10.1021/acs.inorgchem.8b02800
Inorg. Chem. 2019, 58, 637−647